JOURNAL OF PROPULSION AND POWER
Vol. 23, No. 5, September–October 2007

Numerical Study of an Electron-Beam-Confined Faraday Accelerator

Bernard Parent[*]
Nagaoka University of Technology, Nagaoka 940-2188, Japan
Sergey Macheret[†] and Mikhail Shneider[‡]
Princeton University, Princeton, New Jersey 08544-5263
and
Nobuhiro Harada[§]
Nagaoka University of Technology, Nagaoka 940-2188, Japan

DOI: 10.2514/1.26936

The numerical solution of a magnetoplasmadynamics accelerator intended for supersonic airbreathing propulsion systems is presented. The numerical method solves the Favre-averaged Navier–Stokes equations closed by the Wilcox $k\omega$ model, including the nitrogen vibrational energy and a finite rate chemical solver accounting for electron-beam ionization, electron attachment, and dissociative recombination. The fluid-flow equations are solved in conjunction with the electric-field-potential equation. Because of the recombination time of the electrons with the charged particles being in the order of microseconds, the interaction region is more or less confined to the area when e-beam ionization is applied. In this manner, a Faraday-type configuration can be obtained by using only one electrode pair. The impact of the length of the interaction region and the strength of the magnetic field on the efficiency are assessed. It is observed that the efficiency obtained numerically is as much as 40% less than the theoretical predictions for the highest magnetic field considered of 4 T. This is attributed to 1) the current concentration near the electrodes' edges causing a significant voltage drop and 2) unsteady behavior in the center of the channel due to the interaction between finite rate chemistry and electromagnetism. Nonetheless, an efficiency within 25% of the theoretical predictions can be obtained at high magnetic field by decreasing the width of the interaction region to one-tenth of its height.

Nomenclature

$\mathcal{A}$ = Avogadro's number, 6.02257×10^{23}
$\boldsymbol{B}$ = magnetic field vector
b = constant function of γ and K
C = charge, C
C_P = specific heat at constant pressure
c = mass fraction
$\boldsymbol{E}$ = electric field vector
E = total energy
e = charge of one electron, 1.60207×10^{-19} C
e = internal energy
e_v = nitrogen vibrational energy
e_v^0 = nitrogen vibrational energy at equilibrium
h = enthalpy
$\boldsymbol{j}$ = current vector
K = work interaction parameter, $\boldsymbol{E}_y/(\boldsymbol{v}_x\boldsymbol{B}_z)$
k = turbulence kinetic energy
L = length of the interaction region
M = Mach number
$\mathcal{M}$ = molecular weight
m = atom or molecule mass
N = number density
P = pressure
P_k = turbulence kinetic energy production term
Pr = Prandtl number
q = flow speed
q_b = energy deposited to the flow from the electron beams
R = gas constant
Sc = Schmidt number
St = Stuart number, $\sigma_{\text{eff}}\boldsymbol{B}^2L/(\rho q)$
s = sign of a species (-1 for negative ions and electrons and $+1$ for positive ions)
T = temperature
$\boldsymbol{v}$ = velocity vector
W = chemical source term
X = matrix needed to compute the effective conductivity
γ = ratio of the specific heats
δ_{ij} = Kronecker delta
η = efficiency
Θ_v = nitrogen characteristic vibration temperature
κ = thermal conductivity
λ^e = electron thermal diffusion
μ = viscosity, mobility
ν = mass diffusion coefficient
ξ = ratio between the Joule heating and the work
ρ = density
σ = electrical conductivity
$\tilde{\sigma}$ = tensor conductivity
σ_{eff} = effective electrical conductivity taking into account ion slip
σ_k = user-defined constant for the Wilcox $k\omega$ model
σ_ω = user-defined constant for the Wilcox $k\omega$ model
τ_{vt} = vibration-translation relaxation time
ϕ = electric field potential

Presented as Paper 2890 at the Plasmadynamics and Lasers, San Francisco, CA, 5–8 June 2006; received 1 August 2006; revision received 24 January 2007; accepted for publication 23 February 2007. Copyright © 2007 by Bernard Parent, Sergey Macheret, Mikhail Shneider, and Nobuhiro Harada. Published by the American Institute of Aeronautics and Astronautics, Inc., with permission. Copies of this paper may be made for personal or internal use, on condition that the copier pay the $10.00 per-copy fee to the Copyright Clearance Center, Inc., 222 Rosewood Drive, Danvers, MA 01923; include the code 0748-4658/07 $10.00 in correspondence with the CCC.

[*] Japanese Society for the Promotion of Science Researcher, 1603-1 Kamitomioka; bernard.parent@utoronto.ca.

[†] Senior Research Scientist, Department of Mechanical and Aerospace Engineering.

[‡] Research Staff Member, Department of Mechanical and Aerospace Engineering.

[§] Professor, 1603-1 Kamitomioka; nob@nagaokaut.ac.jp.

ω = turbulence kinetic energy specific dissipation rate

Subscripts

t = turbulent
v = vibrational
1 = station 1
2 = station 2

Superscripts

e = electron
k = kth species
$\star$ = turbulent and molecular

Introduction

AIRBREATHING jet engines propulsing present-day aircraft provide thrust through conversion of the heat added chemically into work, which is accomplished by compressing and expanding the fluid before and after the heat addition, respectively. Although this has proven to be a viable concept for flight over a limited Mach number range, extending the flight Mach number envelope of airbreathing jet engines is not a trivial task. Difficulties originate from the complicated compression process in the inlet, which needs to be accomplished with minimal losses. To minimize losses while maintaining a high pressure in the combustor, radical variations in the design/geometry of the engine are needed as the aircraft accelerates from rest to hypersonic speeds.

This prompted the development of substantially different engine designs such as the turbojet, the ramjet, and the scramjet to cover the flight Mach number envelopes 0–3, 3–7, and 7–15, respectively. It follows that to operate from rest to high speeds, the different designs must be combined into one or somehow substituted to one another during flight. Adding to the challenge are the high heat loads characteristic of hypersonic flight, effectively rendering any type of mechanical control on the engine geometry a challenging endeavor.

Magnetoplasmadynamics (MPD) has recently been the focus of substantial interest as a means to improve the performance of supersonic and hypersonic flight vehicles. One possibility that MPD offers is the bypass of the flow kinetic energy from the inlet to the nozzle, such as in project AJAX [1,2] or as in other derived concepts [3,4]. By bypassing some of the flow energy around the combustor through an MPD generator and accelerator, it is foreseen that high-speed propulsion systems could deliver a higher efficiency through a larger Mach number range without requiring significant changes to the engine geometry.

Another application that requires the use of an MPD accelerator is the magnetoplasma jet engine, as first proposed in [5]. As shown in Fig. 1, the engine produces thrust through an MPD accelerator with the energy emanating from a stack of fuel cells. Before entering the fuel cell compartment, the incoming air is decelerated to Mach 1 through an MPD generator to prevent damage to the fuel cells due to shocks. The power generated by the MPD generator and by the fuel cells is then distributed to one MPD accelerator located downstream of the fuel cells and to a second accelerator located in the high-speed duct. The power is split between the two accelerators such that the thrust of the engine is maximized, with most of the power typically being directed to the accelerator in the high-speed duct. The air is ionized with electron beams because it is the most efficient way currently known to sustain ionization in cold air. Quasi-one-dimensional studies [5] indicate that the magnetoplasma jet engine can deliver a specific impulse higher than that of the turbojet or the ramjet in the Mach number range 3–5 without requiring significant changes in the engine geometry.

In this paper, a numerical study of an MPD accelerator using electron-beam ionization is presented. The flow conditions are representative of the MPD accelerator in the high-speed duct of the magnetoplasma jet engine for a flight Mach number of 4 and a dynamic pressure of 50 kPa. A new numerical method is presented to tackle this problem. The method solves the Favre-averaged Navier–Stokes equations closed by the Wilcox $k\omega$ model, including the nitrogen-vibrational-energy transport equation and an eight-species, finite rate, low-temperature air-chemical solver to obtain the electron and ion number densities. The chemical reactions include dissociative recombination and electron attachment, which depend on the electron temperature determined locally from the electric field. The electric field and the current are obtained through the solution of the electric-field-potential equation, including the Hall effect and the ion slip effect. As needed to solve the electric-field-potential equation, the conductivity is obtained from the electron/ion number densities originating from the solution of the fluid-flow equations and from the electron mobility, which is determined locally as a function of the effective electric field.

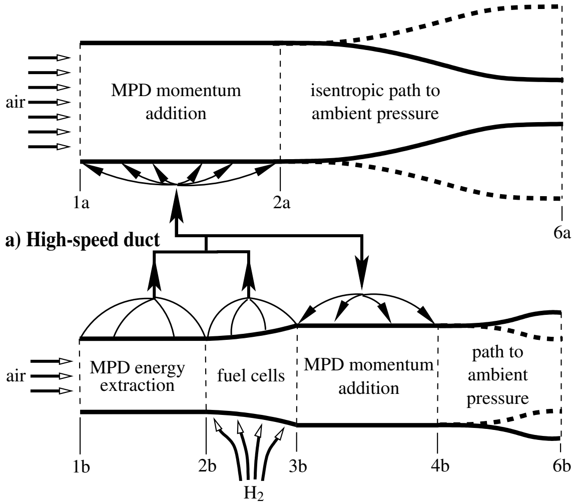

Fig. 1 Schematic of the fuel-cell-powered magnetoplasma jet engine [5].

Governing Equations

Fluid Dynamics

The mass-conservation transport equations for the neutral molecules and the negative/positive ions is fixed to

$$\frac{\partial}{\partial t}\rho c^k + \sum_{j=1}^{d}\frac{\partial}{\partial x_j}\rho v_j c^k - \sum_{j=1}^{d}\frac{\partial}{\partial x_j}\nu^{k\star}\frac{\partial c^k}{\partial x_j} = W^k \tag{1}$$

where c^k is the mass fraction of species k, and W^k are the chemical source terms obtained in the usual form from the set of reactions outlined in Table 1. The effective diffusion coefficient is composed of molecular and turbulent contributions and corresponds to $\nu^{k\star} = \nu^k + \mu_t/Sc_t$, where μ_t is the turbulent viscosity and Sc_t is the turbulent Schmidt number (here, given a value of 1). The molecular diffusion ν^k is determined from Wilke's mixing rule and from the Dixon–Lewis polynomials [12] and also contains a correction to account for ambipolar diffusion: for the ions, the molecular diffusion is multiplied by the factor $1 + T^e/T$, with T^e being the electron temperature. Because the electron temperature can be as much as 100 times higher than the translational energy, the ambipolar diffusion coefficient becomes very high, reaching values that can exceed the turbulence eddy diffusion. This has a large impact on the conductivity, especially in the near-wall regions, in which the turbulence diffusion is small and the electron temperature is large.

No mass-conservation transport equation is solved for the electrons. Rather, the electron number density is obtained from the number density of the other charged particles, assuming a neutral plasma. This is a fair assumption for this problem because the number density of the charged species is sufficiently high for the plasma to be considered neutral.

The momentum equation for the neutrals takes on the following form:

Table 1 An 8-species, 28-reaction, air-chemical model; species consist of e^-, $\mathrm{O_2}$, $\mathrm{N_2}$, O, N, $\mathrm{O_2^+}$, $\mathrm{N_2^+}$, and $\mathrm{O_2^-}$

No.	Reaction	Rate coefficient, 1/s or cm^3/s or cm^6/s	Reference
1a	$e^- + \mathrm{N_2} \to \mathrm{N_2^+} + e^- + e^-$	$10^{-8.3-36.5/\vartheta}$ cm^3/s	[6]
1b	$e^- + \mathrm{O_2} \to \mathrm{O_2^+} + e^- + e^-$	$10^{-8.8-28.1/\vartheta}$ cm^3/s	[6]
2a	$e^- + \mathrm{O_2^+} \to \mathrm{O} + \mathrm{O}$	$2.0 \times 10^{-7}(300/T_\mathrm{e})^{0.7}$ cm^3/s	[7]
2b	$e^- + \mathrm{N_2^+} \to \mathrm{N} + \mathrm{N}$	$2.8 \times 10^{-7}(300/T_\mathrm{e})^{0.5}$ cm^3/s	[8]
3a	$\mathrm{O_2^-} + \mathrm{N_2^+} \to \mathrm{O_2} + \mathrm{N_2}$	$2.0 \times 10^{-7}(300/T)^{0.5}$ cm^3/s	[8]
3b	$\mathrm{O_2^-} + \mathrm{O_2^+} \to \mathrm{O_2} + \mathrm{O_2}$	$2.0 \times 10^{-7}(300/T)^{0.5}$ cm^3/s	[8]
4a	$\mathrm{O_2^-} + \mathrm{N_2^+} + \mathrm{N_2} \to \mathrm{O_2} + \mathrm{N_2} + \mathrm{N_2}$	$2.0 \times 10^{-25}(300/T)^{2.5}$ cm^6/s	[8]
4b	$\mathrm{O_2^-} + \mathrm{O_2^+} + \mathrm{N_2} \to \mathrm{O_2} + \mathrm{O_2} + \mathrm{N_2}$	$2.0 \times 10^{-25}(300/T)^{2.5}$ cm^6/s	[8]
4c	$\mathrm{O_2^-} + \mathrm{N_2^+} + \mathrm{O_2} \to \mathrm{O_2} + \mathrm{N_2} + \mathrm{O_2}$	$2.0 \times 10^{-25}(300/T)^{2.5}$ cm^6/s	[8]
4d	$\mathrm{O_2^-} + \mathrm{O_2^+} + \mathrm{O_2} \to \mathrm{O_2} + \mathrm{O_2} + \mathrm{O_2}$	$2.0 \times 10^{-25}(300/T)^{2.5}$ cm^6/s	[8]
5a	$e^- + \mathrm{O_2} + \mathrm{O_2} \to \mathrm{O_2^-} + \mathrm{O_2}$	$1.4 \times 10^{-29}(300/T_e)\exp(-600/T)\exp([700(T_e - T)/T_e T])$ cm^6/s	[8]
5b	$e^- + \mathrm{O_2} + \mathrm{N_2} \to \mathrm{O_2^-} + \mathrm{N_2}$	$1.07 \times 10^{-31}(300/T_e)^2\exp(-70/T)\exp([1500(T_e - T)]/T_e T)$ cm^6/s	[8]
6	$\mathrm{O_2^-} + \mathrm{O_2} \to \mathrm{e} + \mathrm{O_2} + \mathrm{O_2}$	$8.6 \times 10^{-10}\exp(-6030/T)[1 - \exp(-1570/T)]$ cm^3/s	[9], Chap. 2
7a	$\mathrm{O_2} \to e^- + \mathrm{O_2^+}$	$2.0 \times 10^{17} q_b/N$ 1/s	[10]
7b	$\mathrm{N_2} \to e^- + \mathrm{N_2^+}$	$1.8 \times 10^{17} q_b/N$ 1/s	[10]
8a	$\mathrm{O_2} + \mathrm{O_2} \to 2\mathrm{O} + \mathrm{O_2}$	$3.7 \times 10^{-8}\exp(-59,380/T)[1 - \exp(-2240/T)]$ cm^3/s	[7,11]
8b	$\mathrm{O_2} + \mathrm{N_2} \to 2\mathrm{O} + \mathrm{N_2}$	$9.3 \times 10^{-9}\exp(-59,380/T)[1 - \exp(-2240/T)]$ cm^3/s	[7,11]
8c	$\mathrm{O_2} + \mathrm{O} \to 3\mathrm{O}$	$1.3 \times 10^{-7}\exp(-59,380/T)[1 - \exp(-2240/T)]$ cm^3/s	[7,11]
8d	$\mathrm{N_2} + \mathrm{O_2} \to 2\mathrm{N} + \mathrm{O_2}$	$5.0 \times 10^{-8}\exp(-113,200/T)[1 - \exp(-3354/T)]$ cm^3/s	[7,11]
8e	$\mathrm{N_2} + \mathrm{N_2} \to 2\mathrm{N} + \mathrm{N_2}$	$5.0 \times 10^{-8}\exp(-113,200/T)[1 - \exp(-3354/T)]$ cm^3/s	[7,11]
8f	$\mathrm{N_2} + \mathrm{O} \to 2\mathrm{N} + \mathrm{O}$	$1.1 \times 10^{-7}\exp(-113,200/T)[1 - \exp(-3354/T)]$ cm^3/s	[7,11]
9a	$\mathrm{O} + \mathrm{O} + \mathrm{O_2} \to 2\mathrm{O_2}$	$2.45 \times 10^{-31}T^{-0.63}$ cm^6/s	[7,11]
9b	$\mathrm{O} + \mathrm{O} + \mathrm{N_2} \to \mathrm{O_2} + \mathrm{N_2}$	$2.76 \times 10^{-34}\exp(720/T)$ cm^6/s	[7,11]
9c	$\mathrm{O} + \mathrm{O} + \mathrm{O} \to \mathrm{O_2} + \mathrm{O}$	$8.8 \times 10^{-31}T^{-0.63}$ cm^6/s	[7,11]
9d	$\mathrm{N} + \mathrm{N} + \mathrm{O_2} \to \mathrm{N_2} + \mathrm{O_2}$	$8.27 \times 10^{-34}\exp(500/T)$ cm^6/s	[7,11]
9e	$\mathrm{N} + \mathrm{N} + \mathrm{N_2} \to 2\mathrm{N_2}$	$8.27 \times 10^{-34}\exp(500/T)$ cm^6/s	[7,11]
9f	$\mathrm{N} + \mathrm{N} + \mathrm{O} \to \mathrm{N_2} + \mathrm{O}$	$8.27 \times 10^{-34}\exp(500/T)$ cm^6/s	[7,11]
9g	$\mathrm{N} + \mathrm{N} + \mathrm{N} \to \mathrm{N_2} + \mathrm{N}$	$8.27 \times 10^{-34}\exp(500/T)$ cm^6/s	[7,11]

$$\frac{\partial}{\partial t}\rho v_i + \sum_{j=1}^{d}\frac{\partial}{\partial x_j}\rho v_j v_i - \sum_{j=1}^{d}\frac{\partial}{\partial x_j}\mu^\star\left(\frac{\partial v_i}{\partial x_j} + \frac{\partial v_j}{\partial x_i} - \frac{2}{3}\delta_{ij}\sum_{k=1}^{d}\frac{\partial v_k}{\partial x_k}\right) + \frac{\partial}{\partial x_i}P^\star = \sum_{k=1}^{n_S} C^k N^k(\boldsymbol{E} + \boldsymbol{v}^{\boldsymbol{k}} \times \boldsymbol{B})_i + C^e N^e(\boldsymbol{E} + \boldsymbol{v}^{\mathbf{e}} \times \boldsymbol{B})_i \tag{2}$$

The term on the right-hand side is the Lorentz force in which C^k is the charge (either positive or negative, in coulombs) of the kth species, N^k is the number density, and $\boldsymbol{v}^{\boldsymbol{k}}$ is the velocity vector of the kth species. The effective pressure includes a contribution from the turbulence $P^\star = P + \frac{2}{3}\rho k$, where the pressure is determined assuming a thermally perfect gas:

$$P = \sum_{k=1}^{n_s} R^k \rho c^k T$$

Also, the effective viscosity corresponds to $\mu^\star = \mu + \mu_t$, where μ is determined from Wilke's mixing rule with polynomials for each species found in [12].

The turbulence transport equation is derived from the laminar form (outlined in [13,14]) using a similar approach used to derive the Favre-averaged Navier–Stokes equations outlined in [15]:

$$\tfrac{\partial}{\partial t}\rho e_v + \textstyle\sum_{j=1}^{d}\tfrac{\partial}{\partial x_j}\rho v_j e_v - \textstyle\sum_{j=1}^{d}\tfrac{\partial}{\partial x_j}\left(\kappa_{e_v}^\star\tfrac{\partial T_v}{\partial x_j}\right) = \eta_v|C^e|N^e\mu^e|\boldsymbol{E} + \boldsymbol{v}^e \times \boldsymbol{E}|^2 + \tfrac{\rho}{\tau_{\mathrm{vt}}}(e_v^0 - e_v) \tag{3}$$

where μ^e the electron mobility. Under the Boussinesq approximation, it can be shown that the modeled form of the effective vibrational energy conductivity corresponds to

$$\kappa_{e_v}^\star = \frac{\partial e_v}{\partial T_v}\left(\frac{\mu}{Pr} + \frac{\mu_t}{Pr_t}\right) \tag{4}$$

where Pr_t the turbulent Prandtl number, which is set to the same value as that used in the total-energy transport equation (i.e., 0.9). The fraction of the Joule heating consumed in the excitation of the vibration levels of the nitrogen molecule, η_v, is obtained from the effective electric field in the electron frame of reference, as tabulated in Table 2. The nitrogen vibration energy at equilibrium can be written as a function of the characteristic vibrational temperature of nitrogen [18]: $e_v^0 = R^{N_2}\Theta_v/[\exp(\Theta_v/T_v) - 1]$ and T_v can be obtained from $e_v = R^{N_2}\Theta_v/[\exp(\Theta_v/T_v) - 1]$. The nitrogen characteristic vibration temperature is set to 3353 K [19] and R^{N_2} is set to 296.8 J/(kg · K). The vibration-translation relaxation time (in seconds) can be obtained from [13,14]:

$$\tfrac{1}{\tau_{\mathrm{vt}}} = N \times 7 \times 10^{-16}\exp\left(-\tfrac{141}{T^{1/3}}\right) + N^O \times 5 \times 10^{-18}\exp\left(-\tfrac{128}{T^{1/2}}\right) \tag{5}$$

where the static temperature is expressed in Kelvin and the number density has units of 1/m^3.

For the Wilcox $k\omega$ model [20], the turbulence kinetic energy and the specific-dissipation-rate transport equation correspond to

Table 2 Electron temperature, fraction of energy consumed in the excitation of the vibration levels of the nitrogen molecule, and electron mobility as functions of the effective electric field (from [16] and Chap. 21 of [17])

$\lvert\boldsymbol{E} + \boldsymbol{v}^e \times \boldsymbol{B}\rvert/N$, V · m^2	T^e, K	η_v	$\mu^e\rho$, kg/V · ms
0.1×10^{-20}	2866	0.00004	0.272
0.2×10^{-20}	4549	0.0218	0.200
0.3×10^{-20}	6233	0.1495	0.174
0.4×10^{-20}	7069	0.2968	0.153
0.6×10^{-20}	8677	0.5502	0.127
0.8×10^{-20}	10,051	0.6934	0.112
1.0×10^{-20}	11,256	0.7792	0.101
2.0×10^{-20}	14,227	0.9338	0.083
3.0×10^{-20}	17,198	0.9652	0.078
5.0×10^{-20}	20,337	0.9233	0.069
8.0×10^{-20}	23,045	0.6497	0.058
10.0×10^{-20}	26,140	0.4678	0.055
14.0×10^{-20}	34,434	0.2467	0.053
20.0×10^{-20}	46,874	0.1102	0.051
30.0×10^{-20}	57,904	0.0411	0.048

$$\frac{\partial}{\partial t}\rho k + \sum_{j=1}^{d}\frac{\partial}{\partial x_j}\rho v_j k - \sum_{j=1}^{d}\frac{\partial}{\partial x_j}\mu_k^{\star}\frac{\partial k}{\partial x_j} = P_k - \rho k\omega \tag{6}$$

$$\tfrac{\partial}{\partial t}\rho\omega + \textstyle\sum_{j=1}^{d}\tfrac{\partial}{\partial x_j}\rho v_j\omega - \textstyle\sum_{j=1}^{d}\tfrac{\partial}{\partial x_j}\mu_\omega^{\star}\tfrac{\partial\omega}{\partial x_j} = \tfrac{\omega}{k}\left[\tfrac{5}{9}P_k - \tfrac{5}{6}\rho k\omega\right] \tag{7}$$

where P_k is set as in [21] and where $\mu_k^{\star}$ and $\mu_\omega^{\star}$ correspond to $\mu + \mu_t/\sigma_k$ and $\mu + \mu_t/\sigma_\omega$, respectively, with σ_k and σ_ω user-specified constants set to two. Knowing the turbulence kinetic energy and its specific dissipation rate, the eddy viscosity can be found from $\mu_t = 0.09(\rho k/\omega)$ [20].

The total-energy transport equation in turbulent form is derived from the laminar form, with attention given to ensure its consistency when solved in conjunction with the turbulence kinetic energy and nitrogen-vibrational-energy transport equations. The total energy here refers to the energy of the neutrals and the ions, excluding the energy of the electrons, which is determined locally as a function of the effective electric field:

$$\begin{aligned}
&\frac{\partial}{\partial t}\rho E + \sum_{j=1}^{d}\frac{\partial}{\partial x_j}\Bigg\{v_j(\rho E + P^{\star}) - \kappa^{\star}\frac{\partial T}{\partial x_j} - c^{N_2}\kappa_{e_v}^{\star}\frac{\partial T_v}{\partial x_j}\\
&\quad - \sum_{k=1}^{n_S} h^k \nu^{k\star}\frac{\partial c^k}{\partial x_j} - e_v \nu^{N_2^{\star}}\frac{\partial c^{N_2}}{\partial x_j}\\
&\quad - \sum_{i=1}^{d} v_i \mu^{\star}\left(\frac{\partial v_i}{\partial x_j} + \frac{\partial v_j}{\partial x_i} - \frac{2}{3}\delta_{ij}\sum_{k=1}^{d}\frac{\partial v_k}{\partial x_k}\right) - \mu_k^{\star}\frac{\partial k}{\partial x_j}\Bigg\}\\
&\quad = \sum_{k=1}^{n_S} C^k N^k(\boldsymbol{E} + \boldsymbol{v}^k \times \boldsymbol{B})\cdot\boldsymbol{v} + C^e N^e(\boldsymbol{E} + \boldsymbol{v}^e \times \boldsymbol{B})\cdot\boldsymbol{v}\\
&\quad + \sum_{k=1}^{n_S} |C^k| N^k \mu^k |\boldsymbol{E} + \boldsymbol{v}^k \times \boldsymbol{B}|^2 + |C^e| N^e \mu^e |\boldsymbol{E} + \boldsymbol{v}^e \times \boldsymbol{B}|^2 + q_b
\end{aligned} \tag{8}$$

The first and second terms on the right-hand side correspond to the work due to the Lorentz force, the third term corresponds to the ion Joule heating, and the fourth term corresponds to the electron Joule heating.

The total energy E corresponds to

$$E = \sum_{k=1}^{n_S} c^k e^k + c^{N_2} e_v + k + \frac{1}{2}\sum_{i=1}^{d} v_i^2 \tag{9}$$

The internal energy e^k contains the heat of formation and the translational, rotational, vibrational, and electronic energies at equilibrium. For all species except nitrogen, the translational, rotational, vibrational, and electronic energies are assumed to be at equilibrium at the temperature T; for nitrogen, the vibrational energy e_v is determined from a separate transport equation. The species energy is obtained from the enthalpy $h^k \equiv e^k + R^k T$, which is determined from temperature-dependent polynomials from McBride et al. [22], typically valid for most species in the range $200 \le T \le 20{,}000$ K. It is emphasized that e^{N_2} and h^{N_2}, as well as e and h, do *not* include the nitrogen vibrational energy. Should the temperature exceed the limit for which the polynomials are valid, the species internal energy is assumed calorically perfect in the range exceeding the maximum temperature (either 6000 or 20,000 K, depending on the species). Because the total energy does not include the electron energy, it is important to make sure that the heat added/removed through chemical reactions is appropriately modeled through the difference in the heat of formation between the products and reactants. Because the McBride polynomials are written such that the enthalpy of the electrons is zero at 298 K, no additional source terms are needed. For consistency between the total energy and the nitrogen-vibrational-energy transport equations, the effective thermal conductivity and the Prandtl number need to be set to

$$\kappa^{\star} = C_P\left(\frac{\mu}{Pr} + \frac{\mu_t}{Pr_t}\right) \tag{10}$$

$$Pr = \frac{\mu}{\kappa}\left(C_P + c^{N_2}\frac{\partial e_v^0}{\partial T}\right) \tag{11}$$

where C_P corresponds to $\partial h/\partial T$ (where h does not include the nitrogen vibrational energy) and the molecular thermal conductivity for the mixture κ is determined from the Mason and Saxena relation and polynomials obtained from [12].

Electrodynamics

Because the plasma is assumed neutral, and further assuming that the electron/ion interactions and the electron/ion pressure gradients are negligible compared with the ion/neutral and electron/neutral collisions, the electric-field-potential equation can be shown to be equal to

$$\sum_i \frac{\partial}{\partial x_i}\left(-\sum_j \tilde{\sigma}_{ij}\frac{\partial\phi}{\partial x_j} + \sum_j \tilde{\sigma}_{ij}(\boldsymbol{v}^n \times \boldsymbol{B})_j\right) = 0 \tag{12}$$

from which the electric field can be obtained as $E_j = -\partial\phi/\partial x_j$. The tensor conductivity corresponds to

$$\tilde{\sigma}_{ij} = \sum_{k=1}^{n_S} |C^k| N^k \mu^k [X^k]_{ij}^{-1} + |C^e| N^e \mu^e [X^e]_{ij}^{-1} \tag{13}$$

with the matrix X^k equal to

$$X^k = \begin{bmatrix} 1 & -s^k\mu^k\boldsymbol{B}_3 & s^k\mu^k\boldsymbol{B}_2 \\ s^k\mu^k\boldsymbol{B}_3 & 1 & -s^k\mu^k\boldsymbol{B}_1 \\ -s^k\mu^k\boldsymbol{B}_2 & s^k\mu^k\boldsymbol{B}_1 & 1 \end{bmatrix} \tag{14}$$

where μ^k is the mobility of species k, C^k the charge in coulombs, and s^k is the sign (that is, -1 for the negative ions and $+1$ for the positive ions). The latter takes into account the Hall effect for the electrons and for the ions (i.e., the ion slip).

The electron temperature and the electron mobility are expressed as functions of the effective electric field $|\boldsymbol{E} + \boldsymbol{v}^e \times \boldsymbol{B}|/N^n$ in the electron frame of reference, with the velocity of the electrons (and of other charged particles) fixed to

$$(\boldsymbol{v}^k - \boldsymbol{v}^n)_i = \sum_j s^k \mu^k [X^k]_{ij}^{-1}(\boldsymbol{E} + \boldsymbol{v}^n \times \boldsymbol{B})_j \tag{15}$$

which assumes that the inertia of the ions/electrons and the pressure gradient terms are negligible compared with the electron-neutral collisions. The relationship between the electric field and the mobility/electron temperature is obtained from data tabulated in Chapter 21 of [17], as outlined in Table 2. Determining the electron temperature and mobility in this manner assumes that the convection terms and diffusion terms in the electron-energy transport equation are negligible compared with the electron Joule heating and the electron energy dissipation to the neutrals. This was verified by implementing the electron-energy transport equation (as outlined in [23]) and by comparing with the electron temperature obtained locally from the effective electric field: except in near-wall regions, negligible differences in the electron temperature are discernible; further, a change in the overall efficiency of less than 1% is observed. Determining the effective electric field in the *electron* frame of reference as opposed to the neutral frame of reference is the correct approach, as can be derived from basic principles. Determining the electron temperature and mobility in the electron frame of reference is critical to this problem, because the electron velocity can differ from the velocity of the neutrals by more than one order of magnitude. The ion mobilities are expressed as a function of the gas temperature and total number density, following correlations based on experimental data [24,25].

Numerical Method

The fluid-flow equations are written in generalized coordinates in strong conservation form, following the approach proposed in [26]. The discretization is accomplished through second-order-accurate finite difference central stencils, except for the convection derivative, which is discretized using the Yee–Roe flux-limited method [27,28]. The standalone Yee–Roe scheme is used without an entropy correction term, because its use increases the amount of numerical diffusion in the boundary layer. For a nonideal gas, including the nitrogen-vibrational-energy transport, the eigenvalues of the flux Jacobian (and corresponding eigenvectors) are similar to those outlined in [29], but with the sound speed corresponding to the square root of

$$\partial P/\partial\rho + \tfrac{2}{3}k + \partial P/\partial\rho E(E + P/\rho - \tfrac{1}{3}k - c^{N_2}e_v - q^2)$$

An arithmetic average (as opposed to a Roe-type average) is taken to obtain the convective flux between the nodes. The time accuracy is achieved through dual time stepping [29], and the solution is iterated in pseudotime using a block-implicit approximate-factorization algorithm and a linearization strategy of the viscous terms by Chang and Merkle [30].

The electric-field-potential equation is discretized using a blend of centered and upwinded finite differences to ensure monotonicity. An implicit direct inversion is performed to advance the solution in pseudotime, with convergence reached when the residual of the electric field potential falls below a user-defined threshold.

Validation

The numerical method here outlined is an extension of the WARP code [21,29] (a Favre-averaged chemically reacting scheme for compressible flow), which was validated in detail in [31]. The 2-D and 3-D validation cases include skin friction over a flat plate, the growth of a compressible shear layer, the composition of a hydrogen–air chemically reacting mixing layer, and the mixing performance of a ramp injector.

However, several enhancements to the method are proposed: 1) the electric-field-potential solver, 2) electromagnetic source terms to the momentum and total-energy equations, 3) the nitrogen-vibrational-energy transport equation, and 4) an eight-species, weakly ionized air, finite rate chemical solver. It would be ideal to compare the method against a set of experimental data of air under MPD control and ionized through electron beams for flow conditions similar to those tackled herein. To the authors' knowledge, such experimental data are not yet available, except for one paper in which MPD control is applied to air flowing over a wedge at supersonic speeds [32]; unfortunately, the flow conductivity is not known.

It is hence preferred to validate the additional schemes added to the WARP code through comparisons with exact solutions.

One-Dimensional Flow in a Duct

In [5], an exact solution for the one-dimensional weakly ionized Euler equations is presented for the special case of a constant value of the work interaction parameter. The configuration applicable to this exact solution is shown in Fig. 2. For a given constant magnetic field B_z, the electric field E_y would correspond to $\boldsymbol{E}_y = K\boldsymbol{B}_z\boldsymbol{v}_x$, with K as the work interaction ratio:

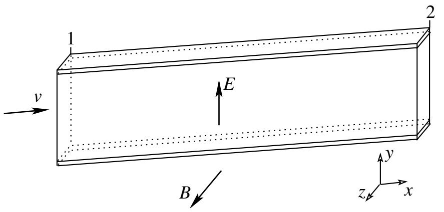

Fig. 2 Schematic of the constant-area duct in which the magnetic field is constant; the electric field vector *E* and the vector *B* × *v* are both parallel to the *y* axis.

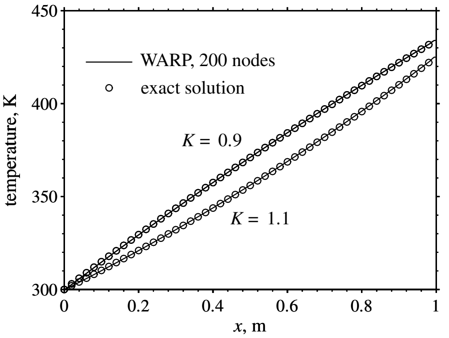

Fig. 3 Comparison of WARP with the exact solution on the basis of temperature in a constant-area duct.

$$K \equiv 1 + \frac{\boldsymbol{j}\cdot\boldsymbol{j}/\sigma}{(\boldsymbol{j}\times\boldsymbol{B})\cdot\boldsymbol{v}} \tag{16}$$

For simplicity, we shall refer to the x component of the velocity as v in this section and denote the flow conditions at the entrance of the duct by the subscript 1. If b is defined as

$$b \equiv \frac{(\gamma+1)K - 2\gamma(K-1)}{\gamma(K-1)(\gamma-1)} \tag{17}$$

then for a specified magnetic field and known conditions at the duct entrance, we can find M as a function of x from:

$$\frac{\sigma\boldsymbol{B}_z^2(x-x_1)}{\rho_1 v_1} = \frac{b\gamma+1}{b(\gamma+1)(K-1)\gamma}\ln\left[\left(\frac{M^2(b-M_1^2)}{M_1^2(b-M^2)}\right)^{\frac{b-1}{b}}\frac{\exp(M^{-2})}{\exp(M_1^{-2})}\right] \tag{18}$$

Knowing the Mach number, the temperature can then be found from the following:

$$\frac{T}{T_1} = \left(\frac{b-M_1^2}{b-M^2}\right)^{\frac{2(b-1)}{b(\gamma+1)}}\left(\frac{M_1}{M}\right)^{\frac{(\gamma-1)2b+4}{b(\gamma+1)}} \tag{19}$$

The temperature as a function of x is plotted in Fig. 3 and compared with the numerical results obtained with the WARP code. The inflow conditions correspond to a Mach number of 6, a pressure of 2 kPa, and a temperature of 300 K. The specific heat ratio and the gas constant are set to 1.4 and 287.06 J/kg · K, respectively, the magnetic field is set to 1 T, and the conductivity to 100 mho/m. WARP is modified so that the electric field is not obtained as a function of the electric field potential, but rather is fixed according to Eq. (16), with the velocity obtained from the temperature and Mach number distributions.

Even using only 200 nodes, the numerical results are in excellent agreement with the exact solution, with no discernible difference observed. A comparison of the velocity and the pressure distributions obtained analytically and numerically also show excellent agreement.

Electric Field Potential in Rectangular Domain with Dirichlet Boundary Conditions

As was performed in [33,34], an exact solution to the electric field potential can be obtained for a rectangular domain with Dirichlet boundary conditions. When the equation

$$\frac{\partial^2\phi}{\partial x^2} + \frac{\partial^2\phi}{\partial y^2} = x\exp(y) \tag{20}$$

is solved on a rectangular domain with the following boundary conditions,

$$\begin{gathered}\phi(0,y) = 0, \qquad \phi(2\text{ m},y) = 2\exp(y), \qquad \phi(x,0) = x\\ \phi(x,1\text{ m}) = x\exp(1)\end{gathered} \tag{21}$$

the analytical solution corresponds to $\phi = x\exp(y)$. To match the

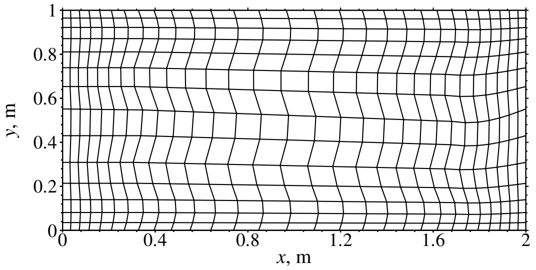

Fig. 4 A 30 × 15 node grid used to obtain the electric field potential with Dirichlet boundary conditions.

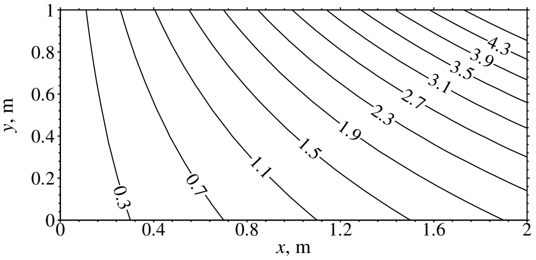

Fig. 5 Contours of the electric field potential in volts obtained using a 30 × 15 node grid.

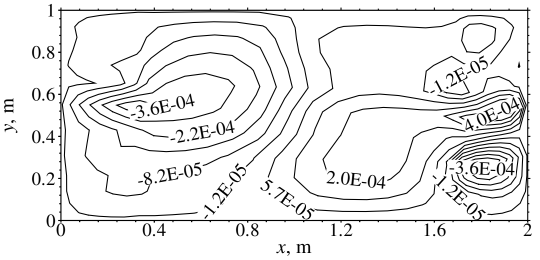

Fig. 6 Contours in volts of the difference between the numerically obtained electric field potential and the exact solution $x\exp(y)$ using a 30 × 15 node grid.

source term in Eq. (20), the magnetic field vector is set to 0, 0, and $\exp(y)/2$ and the velocity vector to x, $-x^2/2$, and 0.

As shown in Fig. 4, the grid is given a sine twist and some clustering along x and y, to test the discretization stencils of ϕ in curvilinear coordinates. The ϕ contours are in very close agreement with the exact solution, with the error typically less than 0.05% (Figs. 5 and 6).

Problem Setup

The problem consists of flow between two electrodes, with the air being ionized externally by electron beams, as shown in Fig. 7. Because of the very fast electron/ion recombination time in air for the flow conditions considered, the conductivity of the plasma drops by an order of magnitude within 1 mm or less. This is expected to contain the current to the region $0.1 \leq x \leq 0.1 + L$ m, hence resulting in a two-electrode Faraday-type accelerator with the width L being user-specified.

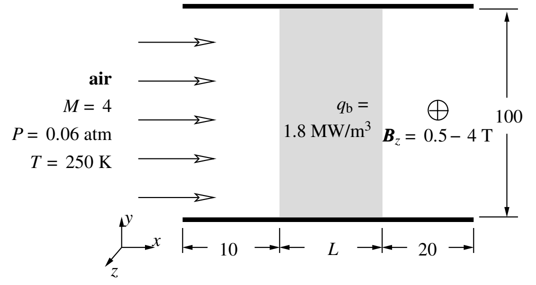

Fig. 7 Design of the Faraday accelerator; all dimensions are in centimeters unless otherwise noted.

The inflow conditions are fixed to a Mach number of 4, a pressure of 0.06 atm, and a temperature of 250 K, yielding a flow speed of 1266 m/s, density of 0.062 kg/m^3, and a Reynolds number of 4.9×10^6 m^{-1}. The voltage between the electrodes is varied such that the total power input to the flow, including the power deposited by the electron beams, is equal to $6.7L$ MW/m depth (the depth being parallel to the z axis). The flow conditions and the power input are representative of those occurring in a 10-m-long high-speed duct part of the magnetoplasma jet engine for a flight Mach number of 4 and a flight dynamic pressure of 50 kPa.

The electron-beam power is fixed for all cases to 1.8 MW/m^3. This yields more or less optimal performance because it is close to being half the amount of Joule heating for the cases considered. Indeed, as was shown in [5], should dissociative recombination be the main electron-loss mechanism, optimal efficiency occurs when the amount of power distributed to the electron beams corresponds to half the amount of Joule heating.

At the wall, the temperature is fixed to 250 K for the translational-energy modes and to adiabatic for the vibrational modes. That is, T is fixed to 250 K and $\partial T_v/\partial y = 0$ at the surface, reflecting a situation in which the fluid can transfer energy directly to the surface only through the translational-energy mode and not the vibrational mode. It is necessary to treat the wall condition for the two energy modes in a different manner, due to the high degree of vibrational nonequilibrium and the surface interacting differently with the translational- and vibrational-energy modes. Because the neutrality of the plasma is enforced throughout the flow, there is no possibility for the formation of plasma sheaths at the walls. This should be a good assumption for this problem, because the thickness of the sheath is expected to be negligibly small compared with the height of the channel (that is, about the same thickness as the laminar sublayer of the turbulent boundary layer). Nonetheless, about 200–300 V could be lost through the plasma sheaths, which would entail a reduction of the efficiency of 3–10% for the problems considered.

Performance Parameters

The efficiency is defined as the integral of the push power divided by the total energy input (including the one originating from e-beam ionization) throughout the domain:

$$\eta \equiv \frac{\int_x \int_y (\boldsymbol{j} \times \boldsymbol{B}) \cdot v \,\mathrm{d}x\mathrm{d}y}{\int_x \int_y (\boldsymbol{E} \cdot \boldsymbol{j} + q_b)\mathrm{d}x\mathrm{d}y} \tag{22}$$

which corresponds to the integral of the work done over the total energy input. It is noted that the integral of the work includes both components of the Lorentz force: one acting in the direction of the flow and the other acting perpendicularly to it. Although the Lorentz force perpendicular to the aircraft line of motion would not instantly create some thrust, it would still result in a momentum increase of the working fluid that could be converted into thrust through interactions with the walls of the engine, depending on how many losses occur when the flow turns in the flight direction. It seems that few losses occur through this process, because the MPD push force predicted by the efficiency closely matches that obtained through the difference between the momentum increase of the fluid in the line of motion and the skin friction.

Defined as the integral of the product between the push force and the flow velocity divided by the total energy input to the flow, the theoretical efficiency is obtained by solving the same governing equations as those used by the numerical method, but by making the following assumptions:

1) The current flows perpendicularly at all times to both the magnetic field and the velocity vectors (that is, as in a Faraday configuration).

2) The flow velocity and the electric/magnetic fields are assumed to remain constant through the interaction process.

The difference in the efficiency obtained theoretically and numerically is hence attributable to the two-dimensional effects, excluding the skin-friction losses.

Numerical Error

Because some unsteadiness is observed in the problem whenever the magnetic field is increased beyond 1 T, all simulations are run enforcing time accuracy using a dual time-stepping method with 60 subiterations. In so doing, it is important to evaluate the error originating from the number of user-defined subiterations. For the situation in which the unsteady effects are seen to be significant (that is, for an interaction length of 10 cm and a magnetic field strength of 4 T), running the same problem using only 20 subiterations per physical time step is seen to affect the efficiency by less than 0.01%. Further, the residual of both the flow equations and the electromagnetic equations decreases by typically four–five orders of magnitude, indicating that a root is obtained at each physical time step.

To determine the numerical error originating from the mesh size, a grid-convergence study is performed for the case of a 10-cm interaction length and a 2-T magnetic field. Four grid levels consisting of 100 × 80, 130 × 104, 169 × 135, and 220 × 176 nodes are investigated. The solution is run in a time-accurate fashion, with the time step decreased as the mesh size is increased. The impact of the mesh size on the efficiency is seen to be very small: as the mesh is increased from 100 × 80 to 220 × 176 nodes, the variation is less than 1%.

Another user-defined grid parameter that can affect the accuracy of the results is the grid spacing at the wall. Because the turbulence model used herein does not make use of wall functions, it is important to locate the first node close enough to the wall to well capture the laminar sublayer of the turbulent boundary layer. For the problems tackled here, the grid spacing at the surfaces is set to 30 μm, which results in a value of y^+ at the wall of approximately four. A similar value of y^+ was observed [21] for the same turbulence model and similar flow conditions to be low enough to well capture the shear stress at the wall and to yield the correct turbulent boundary-layer thickness.

Results

The impact on the efficiency of the magnetic field and the length of the interaction region are assessed in Table 3 and compared with the theoretical prediction in Fig. 8.

As can be observed, the discrepancy between the theoretical and numerical predictions is small at a low magnetic field and becomes more pronounced as the magnetic field is increased. Further, the discrepancy becomes less when the ratio between the height and the length of the interaction region increases. This is attributed to the significant amount of Joule heating taking place at the upstream edge of the cathode and downstream edge of the anode when either the magnetic field or the interaction length is increased.

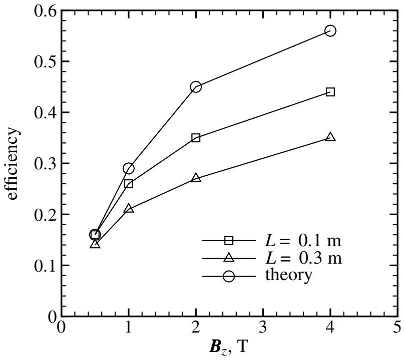

Fig. 8 Comparison of efficiency obtained numerically to that obtained theoretically; the theoretical prediction excludes two-dimensional effects.

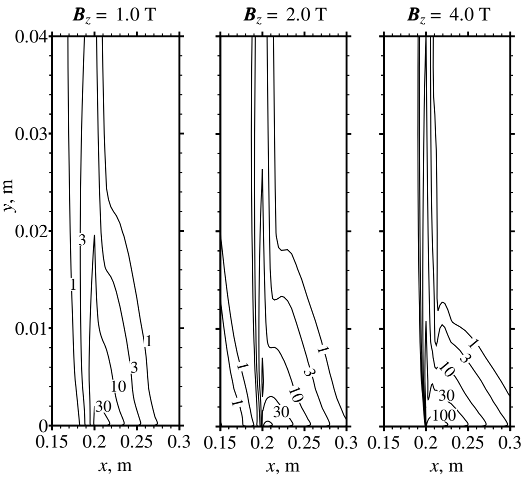

Fig. 9 Ratio of the Joule heating $j \cdot j/\sigma_e$ and the average Joule heating occurring through the domain (as outlined in Table 3, the average Joule heating corresponds to 3.0, 2.4, and 2.0 MW/m^3 for a magnetic field strength of 1.0, 2.0, and 4.0 T). The interaction length L is of 10 cm.

This can be seen through Fig. 9, in which the ratio between the local Joule heating and the average Joule heating throughout the domain is plotted. Two observations can be made:

1) As the magnetic field increases, the Joule heating concentrates on the trailing edge of the anode, due to current concentration caused by the Hall effect.

2) The amount of Joule heating increases by about one order of magnitude from $B_z = 0.5$ T to $B_z = 4.0$ T.

The current concentration does not seem to be impacted significantly by the presence of the boundary layer, because similar current streamlines are obtained for inviscid flow. Similarly, the boundary layer is not affected too significantly by the current

Table 3 Efficiency and thrust as functions of the interaction length and the magnetic field

$\lvert B\rvert$, T	L, m	St[a]	K[b]	Power input, MW	Joule heating, MW	Joule heating within 5 cm of walls, MW	η	Friction drag, N	Force, N	Thrust, N
0.5	0.1	0.24×10^{-3}	4.58	0.64	0.36	0.07	0.16	137.8	80.4	−57.4
1.0	0.1	0.93×10^{-3}	2.84	0.64	0.30	0.09	0.26	135.4	130.1	−5.3
2.0	0.1	3.59×10^{-3}	2.17	0.65	0.24	0.09	0.35	135.5	194.1	58.6
4.0	0.1	12.15×10^{-3}	1.78	0.67	0.20	0.08	0.44	133.5	240.0	106.5
0.5	0.3	0.75×10^{-3}	5.21	2.07	1.24	0.30	0.14	192.0	234.0	42.0
1.0	0.3	3.00×10^{-3}	3.63	2.08	1.11	0.38	0.21	187.5	338.8	151.3
2.0	0.3	11.99×10^{-3}	2.80	2.12	1.00	0.40	0.27	181.1	462.2	281.1
4.0	0.3	40.97×10^{-3}	2.23	2.15	0.85	0.37	0.35	175.5	596.0	420.5

[a] The Stuart number corresponds to $\sigma_{\text{eff}} B^2 L/(\rho q)$, with $q = 1266$ m/s, $\rho = 0.0620$ kg/m^3, and the average effective conductivity σ_{eff} weighted with the magnitude of the current and the cell area.

[b] The load interaction parameter K corresponds to $E_y/(q\lvert B\rvert)$, with E_y set to the difference in potential between the bottom and the top electrodes and q set to the inflow speed of 1266 m/s.

concentration, as can be seen through the comparison of the velocity contours with and without magnetic field near the trailing edge of the anode in Fig. 10, as well as through the skin friction at the wall, shown in Fig. 11. A similar small sudden growth of the boundary layer is also observed near the leading edge of the cathode and is attributed to the decrease of the density due to Joule heating. Nonetheless, because most of the heating is deposited in the form of nitrogen vibrational energy rather than translational energy, the impact on the flow density (and hence the boundary-layer velocity profiles) is small. This is confirmed through the heat transfer rates at the wall, as plotted in Fig. 12: although a significant amount of heat is deposited near the trailing edge of the anode, the heat transfer rate increases by less than 20%, due to the Joule heating being mostly consumed in the excitation of the vibrational levels of nitrogen. The amount of power wasted near the wall in the form of Joule heating can be assessed more or less by taking the integral of $\boldsymbol{j} \cdot \boldsymbol{j}/\sigma_e$ within 5 cm of the surfaces. As shown in Table 3, the amount of Joule heating lost nearby both electrodes accounts for approximately half of the discrepancy between the numerical results and the theoretical prediction.

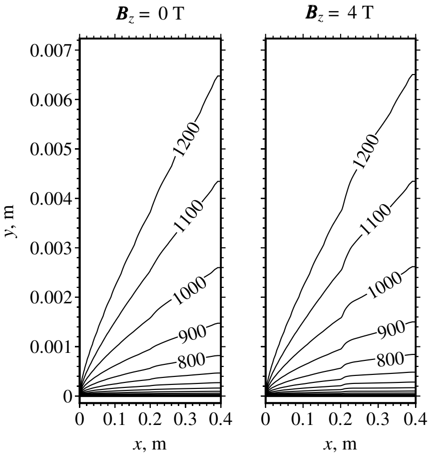

Fig. 10 Contours of the x component of the velocity (m/s) with and without the magnetic field; the interaction length L is of 10 cm.

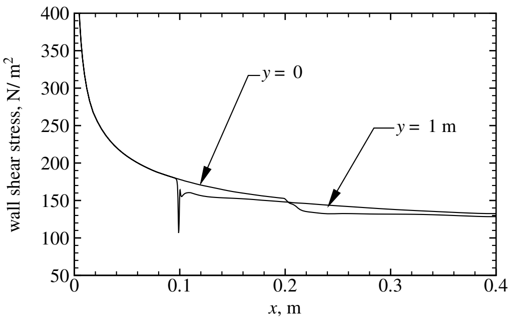

Fig. 11 Shear stress at the wall for a magnetic field of 4 T and an interaction length L fixed to 10 cm (MPD interaction located primarily within $0.1 \leq x \leq 0.2$ m).

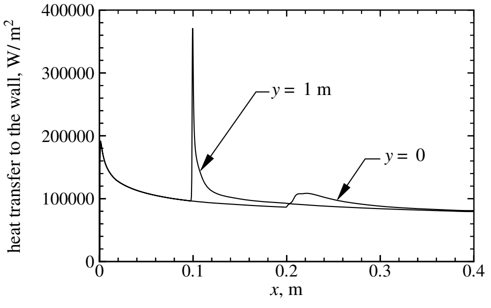

Fig. 12 Heat transfer at the wall for an interaction length L of 10 cm and a magnetic field of 4 T (MPD interaction located primarily within $0.1 \leq x \leq 0.2$ m).

Because the skin friction is not taken into effect when computing the efficiency from the CFD results, it follows that there must be additional losses occurring in the *middle* of the channel that are not predicted theoretically. Indeed, an unexpected phenomenon is seen to occur when the magnetic field is increased beyond 1 T: as shown in Fig. 13, the current does not flow in a smooth vertical manner and exhibits some oscillations in time. This unsteadiness in the solution at a high magnetic field is attributed to the interaction between the finite rate chemistry and the electrodynamic phenomena. For the case of a 4-T magnetic field and a 10-cm-long interaction region, the relevant properties (that is, the electron temperature, the electron number density, and the effective conductivity) are superimposed to the current streamlines in Fig. 14 for one given time step. The flow in the middle of the channel is seen to be striated in regions of high and low electron temperature, with the electron number density varying by about two times from valley to peak.

A particularly interesting feature are the zones of higher conductivity occurring in regions of lower electron number density. Although the conductivity is proportional to the electron number density, it is also proportional to the mobility, which is itself a function of the electron temperature. It is emphasized that the latter is not constant through the domain and varies as a function of the effective electric field in the electron frame of reference. Because of the significant variation of the effective electric field, the electron temperature varies by as much as seven times from valley to peak.

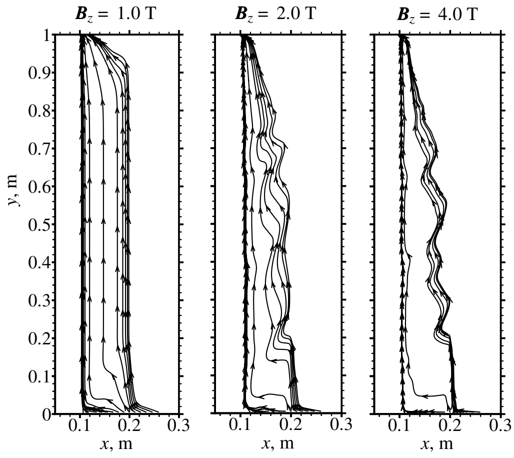

Fig. 13 Current streamlines as a function of the magnetic field for an interaction length L fixed to 10 cm.

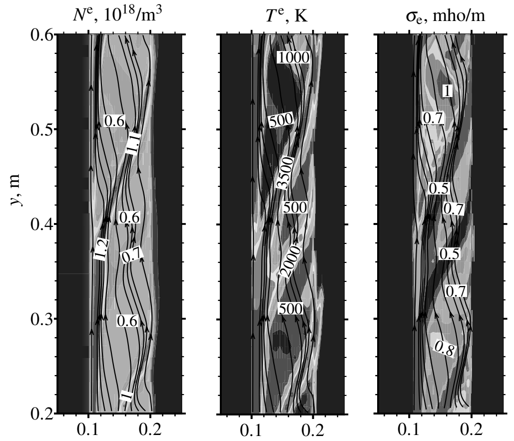

Fig. 14 Electron number density, electron temperature, and effective conductivity for an interaction length L fixed to 10 cm and a magnetic field fixed to 4 T; all data were acquired at the same time level.

This entails a change in the mobility that is substantially more than the variation in electron number density, hence relegating the impact of the latter on the conductivity to a secondary role. As can be observed through the time variation of the properties in Fig. 15, this occurs despite the number density reaching its lowest value when the electron temperature is at its lowest. The tendency of N^e to vary in pair with the electron temperature is attributed to the high rates of recombination and electron attachment (reactions 2a, 2b, 5a, and 5b in Table 1) and their dependency on the electron temperature. Indeed, the recombination and attachment processes yield a relaxation time of about 1 μs, which is of similar magnitude to the time lapse between the peaks of electron temperature and number density.

Along with the current concentration at the electrodes, the unsteady phenomenon occurring at a high magnetic field is postulated to be at the origin of the discrepancy, with the theoretical predictions due to the presence of low-conductivity zones inducing a higher amount of Joule heating losses in the middle of the channel.

Another difficulty encountered at a high magnetic field is the increased induction length necessary for electron–ion recombination, as can be observed through the electron number density contours near the anode in Fig. 16. This might first seem to be due to the higher amount of Joule heating, hence resulting in a higher temperature, which makes the density become lower (a lower flow density increases the electron/ion recombination time and, consequently, the induction length). However, as can be seen through the near-wall temperature contours in Fig. 17, most of the Joule heating is deposited to the flow in terms of nitrogen vibrational energy, which dissipates rather slowly into translational energy. Because the flow density depends directly on the translational temperature and not the vibrational energy, the flow density in the region of high Joule heating decreases negligibly as the magnetic field is raised. Therefore, the high Joule heating is not believed to be the main cause of the longer induction region. Rather, the slower recombination time seems to originate mostly from the higher electron temperature near the anode, as shown in Fig. 18. This effectively reduces the rate of dissociative recombination and electron attachment, hence resulting in a longer induction region.

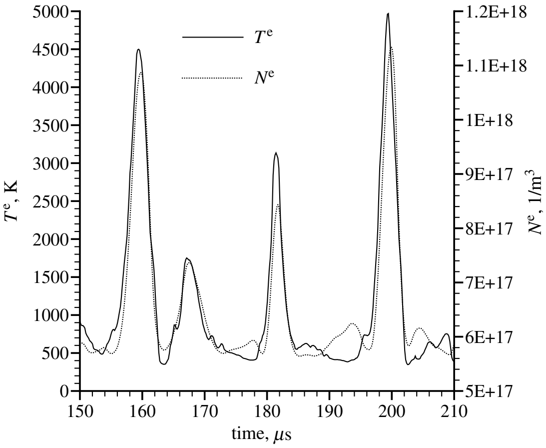

Fig. 15 Time variation of electron temperature and electron number density at $x = 0.15$ m and $y = 0.5$ m for $L = 10$ cm and magnetic field of 4 T.

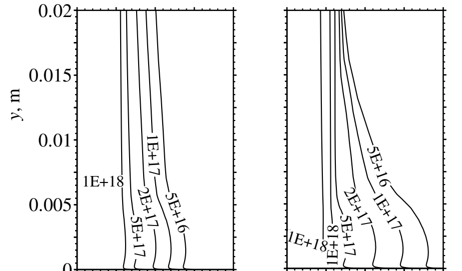

Fig. 16 Electron number density per cubic meter as a function of the magnetic field for an interaction length fixed to 10 cm.

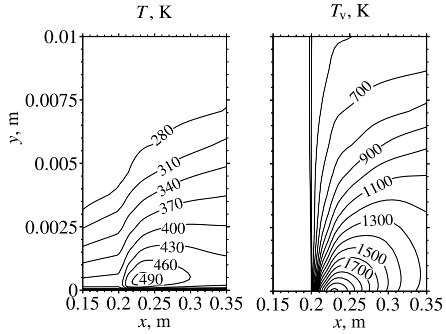

Fig. 17 Temperature and vibrational temperature near the wall for an interaction length fixed to 10 cm and a magnetic field of 4 T.

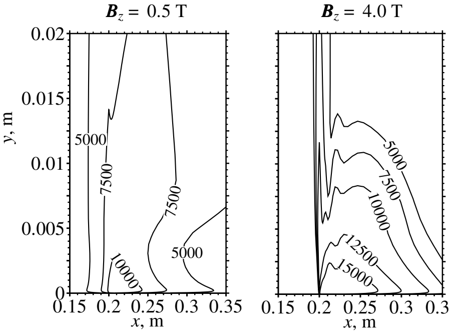

Fig. 18 Electron temperature (in Kelvin) as a function of the magnetic field for an interaction length fixed to 10 cm.

Conclusions

The impact of the magnetic field and the interaction region length on a one-electrode-pair Faraday accelerator confined by e-beam ionization is assessed. It is found that the efficiency obtained numerically can be as much as 40% less than the theoretical predictions when the magnetic field is high. This is attributed to two phenomena, one being voltage drop at the electrodes due to a higher current concentration, and the second being the presence of unsteady waves. The latter occurs only when the magnetic field is raised high enough to cause a significant gradient of the electron temperature at the electrodes.

Nonetheless, the losses induced by the unsteady phenomena and the current concentration at the walls can be minimized by reducing the width of the interaction region: when the latter is reduced threefold, the efficiency reaches 0.44 at a magnetic field of 4 T, which is only 23% less than that of an ideal Faraday accelerator.

Another difficulty encountered is the rather high induction distance occurring at the downstream edge of the anode, especially when the magnetic field is high. The higher electron temperature at a high magnetic field results in a slower recombination of the electrons with the ions, hence resulting in the induction region being 10–15-cm long. This is worrisome because it will probably be necessary to separate the electrode pairs by at least this distance to prevent arcing in a segmented-electrode Faraday accelerator. Because the induction length is of considerable size compared with the width of the interaction region, the length of a segmented-electrode accelerator would need to be considerably longer than predicted through one-dimensional theory.

Acknowledgment

This work was supported by the Japanese Society for the Promotion of Science (JSPS).

References

[1] Gurijanov, E. P., and Harsha, P. T., "AJAX: New Directions in Hypersonic Technology," AIAA Paper 96-4609, 1996.

[2] Kuranov, A. L., Korabelnicov, A. V., Kuchinskiy, V. V., and Sheikin, E. G., "Fundamental Techniques of the AJAX Concept: Modern State of Research," AIAA Paper 2001-1915, 2001.

[3] Vatazhin, A. B., and Kopchenov, V. I., "Problem of Hypersonic Flow Deceleration by Magnetic Field," *Scramjet Propulsion*, edited by E. T. Curran and S. N. B.Murthy, Progress in Aeronautics and Astronautics, Vol. 189, AIAA, Washington, D.C., 2001, pp. 891–938, Chap. 14.

[4] Litchford, R. J., Cole, J. W., Bityurin, V. A., and Lineberry, J. T., "Thermodynamic Cycle Analysis of Magnetohydrodynamic-Bypass Hypersonic Airbreathing Engines," *Journal of Propulsion and Power*, Vol. 17, No. 2, 2001, pp. 477–480.

[5] Parent, B., and Jeung, I.-S., "Fuel-Cell-Powered Magnetoplasma Jet Engine with Electron Beam Ionization," *Journal of Propulsion and Power*, Vol. 21, No. 3, 2005, pp. 433–441.

[6] Raizer, Y. P., *Gas Discharge Physics*, Springer–Verlag, Berlin, 1991.

[7] Aleksandrov, N. L., Bazelyan, E. M., Kochetov, I. V., and Dyatko, N. A., "The Ionization Kinetics and Electric Field in the Leader Channel in Long Air Gaps," *Journal of Physics D: Applied Physics*, Vol. 30, No. 11, 1997, pp. 1616–1624.

[8] Kossyi, A., Kostinsky, A. Y., Matveyev, A. A., and Silakov, V. P., "Kinetic Scheme of the Non-Equilibrium Discharge in Nitrogen-Oxygen Mixtures," *Plasma Sources Science and Technology* , Vol. 1, No. 3, 1992, pp. 207–220.

[9] Bazelyan, E. M., and Raizer, Y. P., *Spark Discharge*, CRC, Boca Raton, FL, 1997.

[10] Bychkov, Y. I., Korolev, Y. D., and Mesyats, G. A., *Inzhektsionnaia Gazovaia Elektronika (Injection Gaseous Electronics)*, Nauka, Novosibirsk, Russia, 1982.

[11] Krivonosova, O. E., Losev, S. A., Nalivayko, V. P., Mukoseev, Y. K., and Shatalov, O. P., *Khimiia Plazmy (Plasma Chemistry)*, edited by B. M. Smirnov, Energoatomizdat, Moscow, Russia, Vol. 14, 1987, p. 3.

[12] Dixon–Lewis, G., "Computer Modelling of Combustor Reactions," *Combustion Chemistry*, edited by W. C. Gardiner, Springer–Verlag, New York, 1984, Chap. 2, pp. 21–125.

[13] Macheret, S. O., Shneider, M. N., and Miles, R. B., "Electron-Beam-Generated Plasmas in Hypersonic Magnetohydrodynamic Channels," *AIAA Journal*, Vol. 39, No. 6, 2001, pp. 1127–1138.

[14] Macheret, S. O., Martinelli, L., and Miles, R. B., "Shock Wave Propagation and Structure in Non-Uniform Gases and Plasmas," AIAA Paper 99-0598, 1999.

[15] Wilcox, D. C., *Turbulence Modeling for CFD*, 2nd ed., DCW Industries, La Cañada, CA, 1998.

[16] Aleksandrov, N. L., Vysikailo, F. I., Islamov, R. S., Kochetov, I. V., Napartovich, A. P., and Pevgov, V. G., "Electron Distribution Function in 4:1 N2-O2 Mixture," *High Temperature*, Vol. 19, No. 1, 1981, pp. 17–21.

[17] Grigoriev, I. S., and Meilikhov, E. Z., *Handbook of Physical Quantities*, CRC, Boca Raton, FL, 1997.

[18] Anderson, J. D., *Hypersonic and High-Temperature Gas Dynamics*, McGraw–Hill, New York, 1989.

[19] Barrow, G. M., *Introduction to Molecular Spectroscopy*, McGraw–Hill, New York, 1962.

[20] Wilcox, D. C., "Reassessment of the Scale Determining Equation for Advanced Turbulence Models," *AIAA Journal*, Vol. 26, No. 11, 1988, pp. 1299–1310.

[21] Parent, B., Sislian, J. P., and Schumacher, J., "Numerical Investigation of the Turbulent Mixing Performance of a Cantilevered Ramp Injector," *AIAA Journal*, Vol. 40, No. 8, 2002, pp. 1559–1566.

[22] McBride, B. J., Zehe, M. J., and Gordon, S., "NASA Glenn Coefficients for Calculating Thermodynamic Properties of Individual Species," NASA TP 211556, Sept. 2002.

[23] Boeuf, J. P., and Pitchford, L. C., "Two-Dimensional Model of a Capacitively Coupled RF Discharge and Comparisons with Experiments in the Gaseous Electronics Conference Reference Reactor," *Physical Review E (Statistical Physics, Plasmas, Fluids, and Related Interdisciplinary Topics)*, Vol. 51, No. 2, 1995, pp. 1376–1390.

[24] Gosho, Y., and Harada, A., "A New Technique for Measuring Negative Ion Mobilities at Atmospheric Pressure," *Journal of Physics D: Applied Physics*, Vol. 16, No. 7, 1983, pp. 1159–1166.

[25] Sinnot, G., Golden, D. E., and Varney, R. N., "Positive-Ion Mobilities in Dry Air," *Physical Review*, Vol. 170, No. 1, 1968, pp. 272–275.

[26] Vinokur, M., "Conservative Equations of Gas-Dynamics in Curvilinear Coordinate Systems," *Journal of Computational Physics*, Vol. 14, No. 2, 1974, pp. 105–125.

[27] Yee, H. C., Klopfer, G. H., and Montagné, J.-L., "High-Resolution Shock-Capturing Schemes for Inviscid and Viscous Hypersonic Flows," *Journal of Computational Physics*, Vol. 88, No. 1, 1990, pp. 31–61.

[28] Laney, C. B., *Computational Gasdynamics*, Cambridge Univ. Press, New York, 1998.

[29] Parent, B., and Sislian, J. P., "The Use of Domain Decomposition in Accelerating the Convergence of Quasihyperbolic Systems," *Journal of Computational Physics*, Vol. 179, No. 1, 2002, pp. 140–169.

[30] Chang, C.-L., and Merkle, C. L., "The Relation Between Flux Vector Splitting and Parabolized Schemes," *Journal of Computational Physics*, Vol. 80, No. 2, 1989, pp. 344–361.

[31] Parent, B., and Sislian, J. P., "Validation of the Wilcox kω Model for Flows Characteristic to Hypersonic Airbreathing Propulsion," *AIAA Journal*, Vol. 42, No. 2, 2004, pp. 261–270.

[32] Bobashev, S. V., Golovachov, Y. P., and VanWie, D. M., "Deceleration of Supersonic Plasma Flow by an Applied Magnetic Field," *Journal of Propulsion and Power*, Vol. 19, No. 4, 2003, pp. 538–546.

[33] Gaitonde, D. V., "A High-Order Implicit Procedure for the 3-D Electric Field in Complex Magnetogasdynamic Simulations," *Computers and Fluids*, Vol. 33, No. 3, 2004, pp. 345–374.

[34] Poggie, J., "Numerical Simulation of Electromagnetic Flow Control for Hypersonic Systems," 11th International Space Planes and Hypersonic Technologies Conference, Orléans, France, AIAA Paper 2002-5182, Sept. 2002.

R. Bowersox
Associate Editor